Rolling contact fatigue crack propagation in nitrided alloyed steels

Marion Le, Fabrice Ville, xavier Kleber, Jean-Yves Buffiere, Jérôme Cavoret, Marie-christine Sainte-catherine, Laurence Briancon

▶ **To cite this version:**

Marion Le, Fabrice Ville, xavier Kleber, Jean-Yves Buffiere, Jérôme Cavoret, et al.. Rolling contact fatigue crack propagation in nitrided alloyed steels. Proceedings of the Institution of Mechanical Engineers, Part J: Journal of Engineering Tribology, 2017, 231 (9), pp.1192–1208. 10.1177/1350650117717824 . hal-01669929

HAL Id: hal-01669929
https://hal.science/hal-01669929

Submitted on 11 Aug 2023

HAL is a multi-disciplinary open access archive for the deposit and dissemination of scientific research documents, whether they are published or not. The documents may come from teaching and research institutions in France or abroad, or from public or private research centers.

L'archive ouverte pluridisciplinaire **HAL**, est destinée au dépôt et à la diffusion de documents scientifiques de niveau recherche, publiés ou non, émanant des établissements d'enseignement et de recherche français ou étrangers, des laboratoires publics ou privés.

Rolling contact fatigue crack propagation in nitrided alloyed steels

Marion Le[1,2,3], Fabrice Ville[1], Xavier Kleber[2],
Jean-Yves Buffière[2], Jérôme Cavoret[1],
Marie-Christine Sainte-Catherine[4] and Laurence Briancon[3]

Abstract
Experimental investigations were carried out to better understand the rolling contact fatigue mechanisms in nitrided layers of the 33CrMoV12-9 steel grade. Surface-initiated pitting failure mode was reproduced on a twin-disc machine to analyse crack growth and compressive residual stress behaviour within the nitrided layers. Metallographic examinations, 3D observations by means of high-resolution X-ray computed tomography and residual stress analysis were realised on nitrided 33CrMoV12-9 specimens before and after rolling contact fatigue tests. The study revealed that if the initial compressive residual stresses associated with the surface treatment are released during the process of rolling contact fatigue, pre-existing superficial cracks propagate in the nitrided layers along the intergranular carbides. These precipitates induced by the nitriding process therefore act as preferential crack propagation sites.

Keywords
Rolling contact fatigue, surface-initiated pitting, nitriding, microstructure, compressive residual stresses, gears, rolling element bearings, twin-disc machine, crack mechanisms

Introduction

Lots of mechanical engineering components such as gears and rolling element bearings are subjected to rolling contact fatigue (RCF) characterised by high repeated stresses at their rolling surfaces in contact. If contact stresses exceed the material resistance, crack nucleation can occur. Crack propagation toward the component surfaces then leads to material flaking damages called micropitting and pitting (or flaking), that are detrimental for the component lifespan.

Classical structural fatigue and fracture theories are well established by many studies led to correctly explain and predict crack mechanisms.[1] These theories cannot be directly applied to RCF failure modes for different reasons, amongst others:

1. Stress fields induced by contacts are localised near component surfaces, multiaxial, extremely high and characterised by a high hydrostatic stress component.[2] Moreover, during a load RCF cycle, the principal stress axes change in direction.
2. Environmental parameters such as lubrication,[3,4] hydrogen embrittlement,[5] etc. influence the crack mechanisms
3. Material characterisctis (microstructures and compressive residual stresses induced by RCF) affect not only crack initiation as in classical fatigue, but particularly crack propagation.[6,7]

For at least these reasons, RCF issues are specific to each mechanical applications, which have to be invastigated taking into account the whole influencing contact parameters in order to well understand behaviours to failures.

Surface hardening techniques are used to prevent from RCF failure modes. The thermochemical gas-nitriding treatment, studied in this paper, enhances the superficial mechanical properties. Hardness increase and compressive residual stress introduction within the thin and superficial nitrided layers are known to inhibit fatigue crack nucleation and growth.[8,9] However, the process of nitriding induces precipitation of intergranular carbide networks within

[1]LaMCoS, INSA de Lyon, France
[2]Mateis, INSA de Lyon, France
[3]DCNS Research, France
[4]DGA, France

Corresponding author:
Fabrice Ville, LaMCoS, INSA de Lyon, 18-20 rue des Sciences, Villeurbanne Cedex, 69621, France.
Email: fabrice.ville@insa-lyon.fr

the nitrided layers for the majority of alloys, for example the 33CrMoV12-9 steel grade widely used for gears and rolling element bearings. These precipitates are specifically localised at prior austenite grain boundaries (PGB) parallel to surface components.[10] Besides, as a carbon-rich tough and fragile phase, they have been often considered as defects although there is no evidence of this in the literature as introduced in the previous paper.[11] It was also shown that structural fatigue on nitrided steels was widely studied and little has been done on RCF. Moreover, the few RCF investigations mainly focused on the influence of the nitrided depth parameter on the specimen durability and crack mechanisms in comparison with the nitrided microstructure and mechanical properties were not analysed.

Primary investigations, led by the authors and reported in this paper, aimed to address this issue using a twin-disc machine. It was shown that the intergranular carbides tend to make crack propagation easier. This explains the RCF endurance dissimilarities of two nitrided layers displaying different carbide network morphologies but similar mechanical properties (hardness and compressive residual stresses).

The purpose of this paper is to confirm these previous statements studying two other nitrided layer microstructures and analysing a 3D crack network in relation to the intergranular carbides. Concurrently, behaviour during RCF tests of the compressive residual stresses induced by the treatment is examined. RCF crack propagation mechanisms in nitrided 33CrMoV12-9 alloyed steels are finally proposed with respect to the operating contact conditions, the effects of the intergranular carbides and compressive residual stresses.

Experimental methodologies

Test rig and contact conditions

Experiments were performed on a twin-disc machine[12] comprising a first nitrided 33CrMoV12-9 (Table 1) disc to be examined (called *specimen*) in contact with a counter through-hardened 100Cr6 disc, these material beeing widely used in gear and rolling element bearing applications.

In order to analyse the crack behaviour throughout the nitrided layers, RCF tests have been led to reproduce specifically pitting initiated near the surface (i.e. surface-initiated pitting), which is a common failure mode more and more encountered in gear and bearing applications. To do so, each experiment is decomposed into two stages to (1) initiate cracks near the surface and (2) make them propagate throughout the nitrided layers.

Table 1. Chemical composition of 33CrMoV12-9 steel grade.

Chemical element	C	Si	V	Cr	Mn	Ni	Mo
Wt%	0.33	0.34	0.34	3.06	0.58	0.05	0.88

The first so-called *initiation phase* aims at triggering controlled crack nucleation localised at around 30 μm under the extreme surface. Precisely, calibrated dents were realised on the counter 100Cr6 discs used during this *initiation stage*. Those dents act as surface stress raisers when they pass into the contact[13–15] and force surface crack nucleation. To prevent other non-expected surface crack initiation, the specimens were sufficiently ground to remove the extreme thin and brittle compound layer induced by gas-nitriding, as mostly done in gear application. The discs were also surface-finished to obtain smooth surfaces featured by longitudinal roughnesses of $Ra = 0.05\,\mu m$, so that the surface crack initiation coming from machining asperities are avoided.[16–18] The *initiation stage* duration was fixed at the number of cycles required to generate the first observable surface cracks (that will be called "micropitting" in this paper) on the nitrided disc surfaces so as to confirm the presence of RCF defects within the specimens for the rest of the tests.

The following longer *propagation phase* consists in making the initiated cracks propagate throughout the nitrided layers using, in this case, another smooth counter disc without surface stress raisers (i.e. the artificial dents). The operating Hertzian contact pressure given in Table 2 was calculated to get an appropriate contact shear stress field (Figure 1) in relation to the tested nitrided layer mechanical and microstructural properties (these properties are detailed thereafter in section "Effect of nitriding on

Table 2. RCF test contact conditions.

Parameter	Operating contact conditions
Material	Specimen: Gas-nitrided 33CrMoV12-9 Counter disc: Through hardened 100Cr6
Lubrication	Mineral oil ($\upsilon_{40\,^\circ C} = 69$ cSt – $\upsilon_{100\,^\circ C} = 9.3$ cSt) Oil temperature, $T = 80\,^\circ C$ Oil jet. Magnet filters to capture debris
Roughness	$Ra = 0.05\,\mu m$
Speeds	Specimen speed, $v_s = 10.63$ m/s Counter disc speed $v_{cd} = 11.35$ m/s
Slide-to-roll ratio	$SRR = 0.5*(v_{cd} - v_s)/(v_{cd} + v_s) = 6.6\%$
Normal load	$F = 9000$ N
Maximum Hertz pressure	$P_{Hmax} = 2.1$ GPa
Specimen radius	$Rx_s = Rx_{cd} = 35$ mm
Specimen radius of curvature	$Ry_s = 200$ mm; $Ry_{cd} = \infty$
Elliptical contact geometry	$a = 3.08$ mm; $b = 0.65$ mm

different grain size 33CrMoV12-9 alloys''). Maximum Hertzian shear stresses are therefore willingly applied at depths close to the interface of the nitrided cases and the substrate, the purpose was more exactely to observe crack behaviour from the surface throughout the nitrided layers.

Specimen speeds were defined with respect to surface roughness and lubricant properties to operate under full-film lubrication so that damages not linked to RCF failure modes should not appear. The specimens were crowned with a radius of curvature of 200 mm to eliminate the unexpected loading edge effects and to overcome any misalignement. The nitrided discs operated with the lowest speed to accelerate the apparition of micropitting and crack propagation, shortening therefore the experiment duration.[19] Interruptions were carried out to check surface damage evolution along each experiment. The tests were at the end either willingly interrupted or automatically stopped by electromagnetic sensors that detect surface-initiated pitting failure mode.

In order to observe the behaviour of the preexisitng compressive residual stresses within the nitrided layers and their influences on the crack propagation with respect to Hertzian pressures, other experiments were carried out at $P_{Hmax} = 1.2$ GPa and $P_{Hmax} = 2.4$ GPa. Operating contact conditions that vary are highlighted in Table 3.

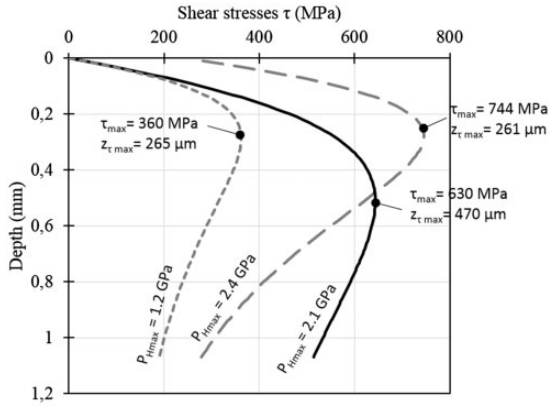

Figure 1. Shear stress profiles at the contact centre induced by different maximum Hertzian pressures $P_{Hmax} = 2.1$, $P_{Hmax} = 1.2$ GPa and $P_{Hmax} = 2.4$ GPa.

These maximum Hertzian pressures were chosen to apply different contact shear stress fields to the superficial volume subjected to RCF compared with experiments at $P_{Hmax} = 2.1$ GPa. Theoretical maximum shear stress values (τ_{max}) and depths ($z_{\tau\ max}$) are shown in Figure 1. These contact conditions were choosen so that for both Hertzian pressures ($P_{Hmax} = 1.2$ GPa and $P_{Hmax} = 2.4$ GPa):

- maximum shear stress depths are comparable
- maximum shear stress levels are different

Metallographic analysis and hardness profile assesments

At the end of the experiments, damaged samples to be analysed were extracted from the nitrided discs with a cut-off wheel machine (Figure 2(1)). These samples were mounted in an epoxy resin and progressively polished in the direction of the disc axis from coarse SiC papers to diamond suspensions (Figure 2(2)). Crack analyses in the samples were led on these cross-sections parallel to the rolling plane (Figure 2(2)). Nital 2% and Béchet-Beaujard etchants were used to properly reveal the nitrided layer microstructures. Hardness profiles were assessed on cross-sections similarly prepared but perpendicular to the rolling plane.

3D observation using high-resolution X-ray computed tomography

For 3D analysis, one of the samples in the presence of RCF damages was reduced to a smaller volume containing half of a crack network as illustrated on Figure 3 where ''b'' denotes the contact half-width in the axial direction. High-resolution X-ray tomography was used to observe this non-destructed remaining part of the crack network inside the sample, by collecting non-absorbed X-ray going through the volume.[20] More precisely, loads of 2D scanned images of the sample in different positions were recorded by a sensor and computed to generate a 3D reconstructed

Table 3. Contact conditions of experiments with $P_{Hmax} = 1.2$ GPa and $P_{Hmax} = 2.4$ GPa compared with the previous tests with $P_{Hmax} = 2.1$ GPa.

P_{Hmax} (GPa)	Normal load (N)	Specimen and counter disc radius (mm)	Specimen and counter disc radius of curvature (mm)
2.1	9000	$Rx_s = 35$ mm $Rx_{cd} = 35$ mm	$Ry_s = 200$ mm $Ry_{cd} = \infty$
1.2	**1600**	$Rx_s = 35$ mm $Rx_{cd} = 35$ mm	$Ry_s = 200$ mm $Ry_{cd} = \infty$
2.4	**1600**	$Rx_s = 35$ mm $Rx_{cd} = 35$ mm	$Ry_s = 200$ mm **$Ry_{cd} = 17.5$ mm**

Bold values corresponds to parameters that were changed to vary contact conditions

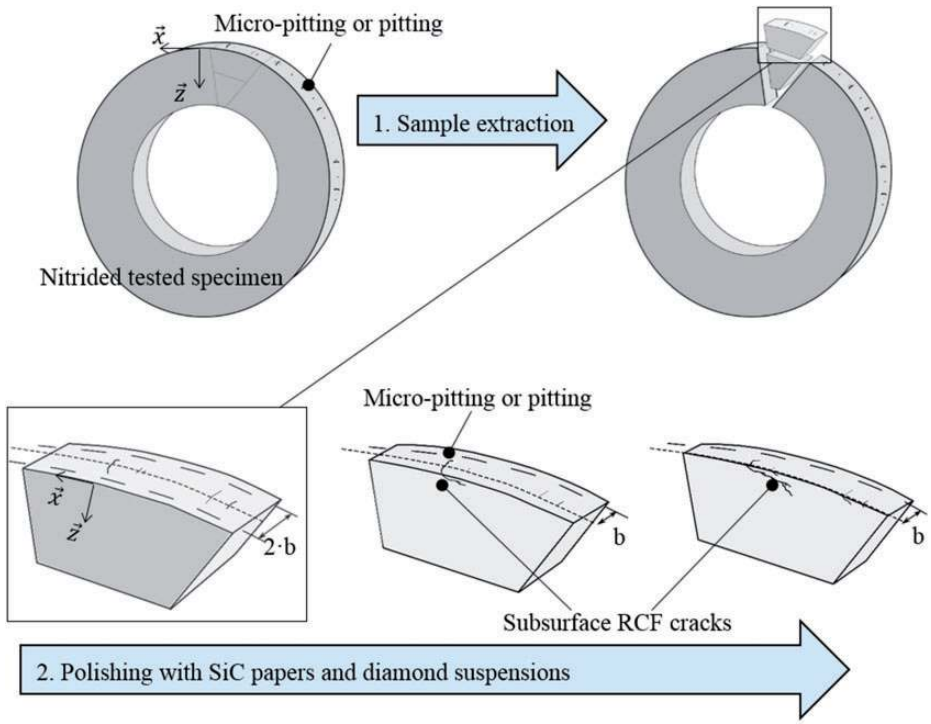

Figure 2. Cross-section preparation for metallographic analysis: (a) sample extraction and (b) polishing procedure. $\vec{x}$ and $\vec{z}$ correspond respectively to the rolling and depth directions. "b" denotes the contact half-width in the axial direction.

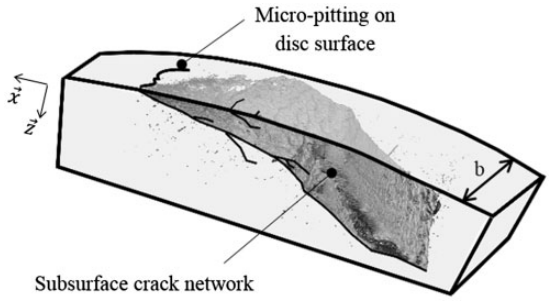

Figure 3. 3D representation of half of a crack network within a damaged sample. $\vec{x}$ and $\vec{z}$ correspond respectively to the rolling and depth directions. "b" denotes the contact half-width in the axial direction.

image of the damaged volume in the presence of RCF cracks. This methodology enables to discretise the analysed $1 \times 1 \times 2$ mm^3 volume with a resolution of 0.7 µm/voxel (3D pixel). Adequate image processing finally allows to retrieve only the crack network without the solid.

Compressive residual stress analysis

Compressive residual stresses before and after RCF tests were assessed throughout the nitrided layers of control samples and discs using X-ray diffraction technique. To do so, repetitive electropolishing was done to remove 100 µm material thickness from the surface toward the substrate. Residual stresses were analysed at these various depths, that is to say at each 100 µm material removal step.

Effect of nitriding on different grain size 33CrMoV12-9 alloys

Disc microstructures before nitriding

Nitrided specimen manufacturing process is summarised in Table 4. The specimens were preliminarily heat-treated before gas-nitriding. Heat treatment experiments on 33CrMoV12-9 alloy were made to observe grain growth according to the austenitisation duration and temperature (Figure 4).

Nitrided microstructures depending on prior austenite grain sizes, four different austenitisation temperatures (T_A) were chosen from the heat treatment experiment results to obtain four batches of specimens with four grain sizes. Austenitisation time was set to 1 h ($t_A = 1$ h) for these four batches. According to the ASTM grain indexes, resulting grain sizes are $G_{ASTM} = 10$, $G_{ASTM} = 8$, $G_{ASTM} = 7$ and $G_{ASTM} = 3$. Corresponding austenitisation temperatures and mean grain diameters are given in Table 4 and illustrated in Figure 5. It is to be noticed that these different grain sizes, apart from $G_{ASTM} = 3$ are in accordance with the gear material quality standard.[21]

After austenitisation, the specimens were all water quenched and tempered at 650 °C for 3 h to release stresses induced by cooling. The discs were machined to remove possible decarburisation layer induced by

Table 4. Nitrided disc manufacturing process.

Manufacturing process	ASTM grain indexes		G_{ASTM}= 10	G_{ASTM}= 8	G_{ASTM}= 7	G_{ASTM}= 3
	Mean grain diameter (μm)		11	20	30	120
	Heat-treatments	Austenitisation (t_A = 1h)	T_{A4}= 900°C	T_{A3}= 975°C	T_{A2}= 1000°C	T_{A1}= 1100°C
		Quenching	Water			
		Tempering	t_T= 3h - T_T= 650°C			
	Machining		Decarburisation layer removal			
	Surface treatment		Gas-nitriding (confidential process parameters)			
	Surface-finishing		Polishing (Ra= 0.05 μm)			

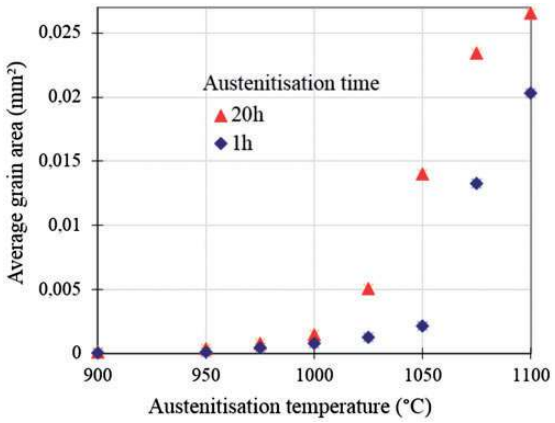

Figure 4. Results of heat treatment tests giving grain size (average area) with respect to the austenitisation duration and temperature.

previous heat treatments. All of the batches were then gas-nitrided at the same time in the same furnace to ensure that no scattering results were potentially induced by the thermochemical heat treatment. The nitrided specimens were finally surface-finished to obtain a roughness parameter of $Ra = 0.05\,\mu m$ as aforementioned.

Microstructural and mechanical properties after nitriding

Observations of the nitrided layer cross-sections (perpendicular to disc surfaces) of each batch outline nitrided microstructure differences (Figure 6(a)). Thin grain-nitrided specimens exhibit networks of intergranular string-shaped carbides that are thin, small, in high density and homogeneously distributed. Coarser grain microstructures rather display thicker and longer carbides, less homogeneously precipitated and in lower density throughout the nitrided layers.

On cross-sections parallel to disc surfaces (Figure 6(b)), intergranular carbide morphologies are different since they precipitate at grain boundaries rather parallel to the disc surfaces. They either appear as white rings surrounding sectioned grains, or white spots on non-sectioned grains (depending on whether the observed micrographies have sectioned grains or not). These surface-parallel cross-sections confirm carbide distribution differences observed on the different grain size nitrided microstructures, as afore-revealed on perpendicular cross-sections to disc surfaces.

Finally, it is worth mentioning that these intergranular carbides are not spread throughout the whole nitrided layers for all the microstructures as arrowed on Figure 7.

Hardness profiles of the different nitrided layers are equivalent (Figure 8), hardness being attributed to the presence of nitrides and not the grain size of the sample. The limit of the nitrided layer being the depth where the hardness is greater than the core's by 100 HV, nitrided layer thicknesses are 500 μm for all the specimens of different grain sizes (±5.5% uncertainty on the hardness measurements is to take into consideration).

Compressive residual stress profiles of the $G_{ASTM} = 10$ and $G_{ASTM} = 7$ microstructures measured on control samples are comparable as depicted on Figure 9. Even if nitrided microstructures of G_{ASTM}=8 and $G_{ASTM} = 3$ were not analysed, it was as well shown in the literature[22] that the grain size does not affect the final residual stress state induced by nitriding. It will therefore be assumed that the compressive residual stress profiles after nitriding are equivalent for all the specimen batches investigated in this study.

In other words, gas-nitriding induces equivalent mechanical properties to all of the specimens despite their different grain sizes. The four specimen batches investigated herein therefore display same mechanical properties (hardness and compressive residual stress profiles) despite their microstructure differences (carbide morphologies and grain sizes) induced by the thermomechanical gas nitriding treatment.

RCF test results at $P_{Hmax} = 2.1$ GPa: Influence of intergranular carbides on crack propagation and compressive residual stress release

Endurances of the tested nitrided microstructures

Results of experiments carried out at $P_{Hmax} = 2.1$ GPa (the other contact conditions are given in Table 2) of

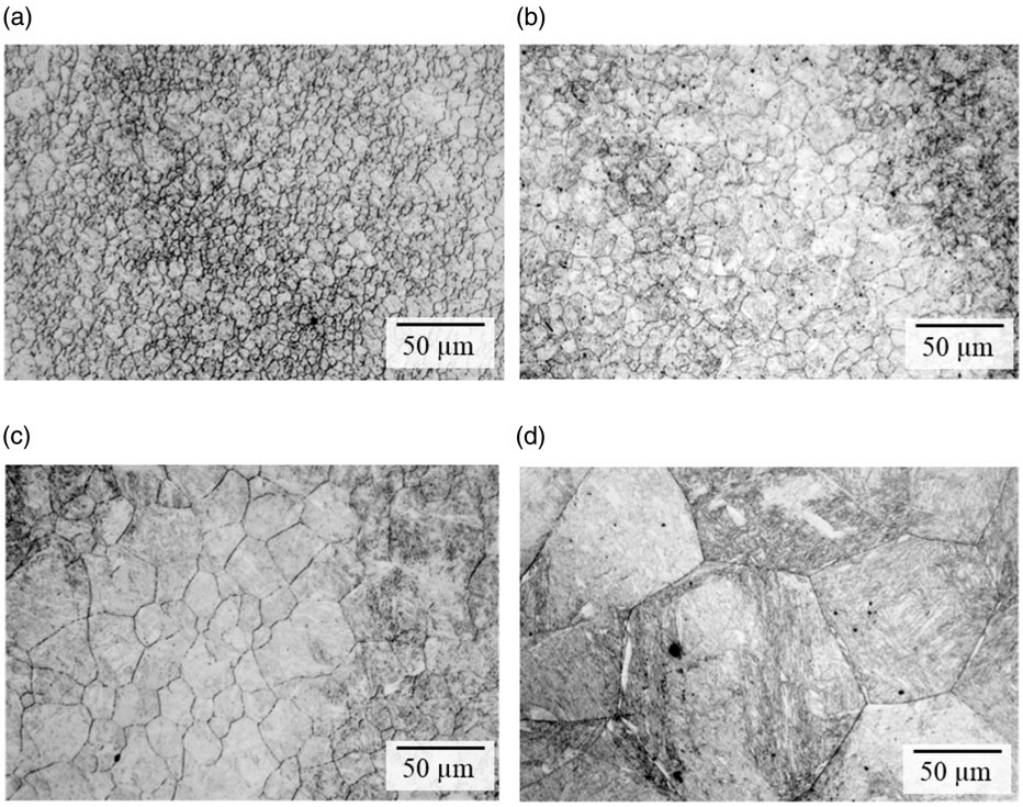

Figure 5. Different chosen grain size steels for RCF tests: (a) $G_{ASTM} = 10$, Mean grain diameter = 11 μm, $T_{A4} = 900\,^{\circ}C$; (b) $G_{ASTM} = 8$, Mean grain diameter = 20 μm, $T_{A3} = 975\,^{\circ}C$; (c) $G_{ASTM} = 7$, Mean grain diameter = 30 μm, $T_{A2} = 1000\,^{\circ}C$; (d) $G_{ASTM} = 3$, Mean grain diameter = 120 μm, $T_{A1} = 1100\,^{\circ}C$.

$G_{ASTM} = 10$ (test no. 1 in Table 5) and $G_{ASTM} = 7$ (tests no. 3 and no. 4) nitrided microstructures are detailed in the previous author's paper.[11] $G_{ASTM} = 8$ nitrided microstructures tested here (test no. 2 in Table 5) showed similar results. The tests also ended as soon as prior stages of pitting failure mode arised (as already observed in previous studies for $G_{ASTM} = 10$ and $G_{ASTM} = 7$). Indeed, electromagnetic sensors set up on the machine and adequate continuous processing of the resulting signals allow to detect surface uplifts (Figure 10(a) to (c)), which is related with an upcoming material flaking (i.e pitting failure mode) that would occur if the tests were run a few more fatigue cycles. It is interesting to notice that for each nitrided disc, only one surface uplift was observed on the whole specimen circumference and in the vicinity of a specific micropit that was initiated during the test initiation phase. These peculiar micropits did not display any surface evolution during the whole test propagation phases, but they lightly broadened only at the end of the experiments (Figure 10(d)). They are more exactely very thin and display no material flaking during the whole RCF tests, contrary to other observed micropits, as if material detachment would have released stresses at crack tips freezing their propagation. As expected (section "Test rig and contact conditions"), surface-initiated pitting were therefore reproduced with subsurface crack propagation and no crack ramifications toward the surface.

Concerning $G_{ASTM} = 3$ (tests nos. 5 and 6 in Table 5), surface-initiated pitting took place as well, but failures gradually developed during fatigue cycling on the nitrided disc surfaces as illustrated on Figure 11. Unlike $G_{ASMT} = 10$, $G_{ASMT} = 8$ and $G_{ASTM} = 7$, subsurface cracks therefore seemed to superficially propagate leading to sooner crack ramifications toward the surfaces of coarse $G_{ASTM} = 3$ nitrided microstructure specimens.

Finally, Table 5 indicates the number of fatigue cycles before surface-initiated pitting apparition on the disc surfaces of the tested microstructures. The coarser the nitrided microstructures are, the lower is the resistance to the RCF failures. Analysis of cross-sections are now required to better understand why the tested nitrided microstructures, featuring similar mechanical properties, display different RCF responses.

2D cross-section observations near the contact centre

Crack behaviour with respect to the nitrided layer mechanical and microstructural properties were

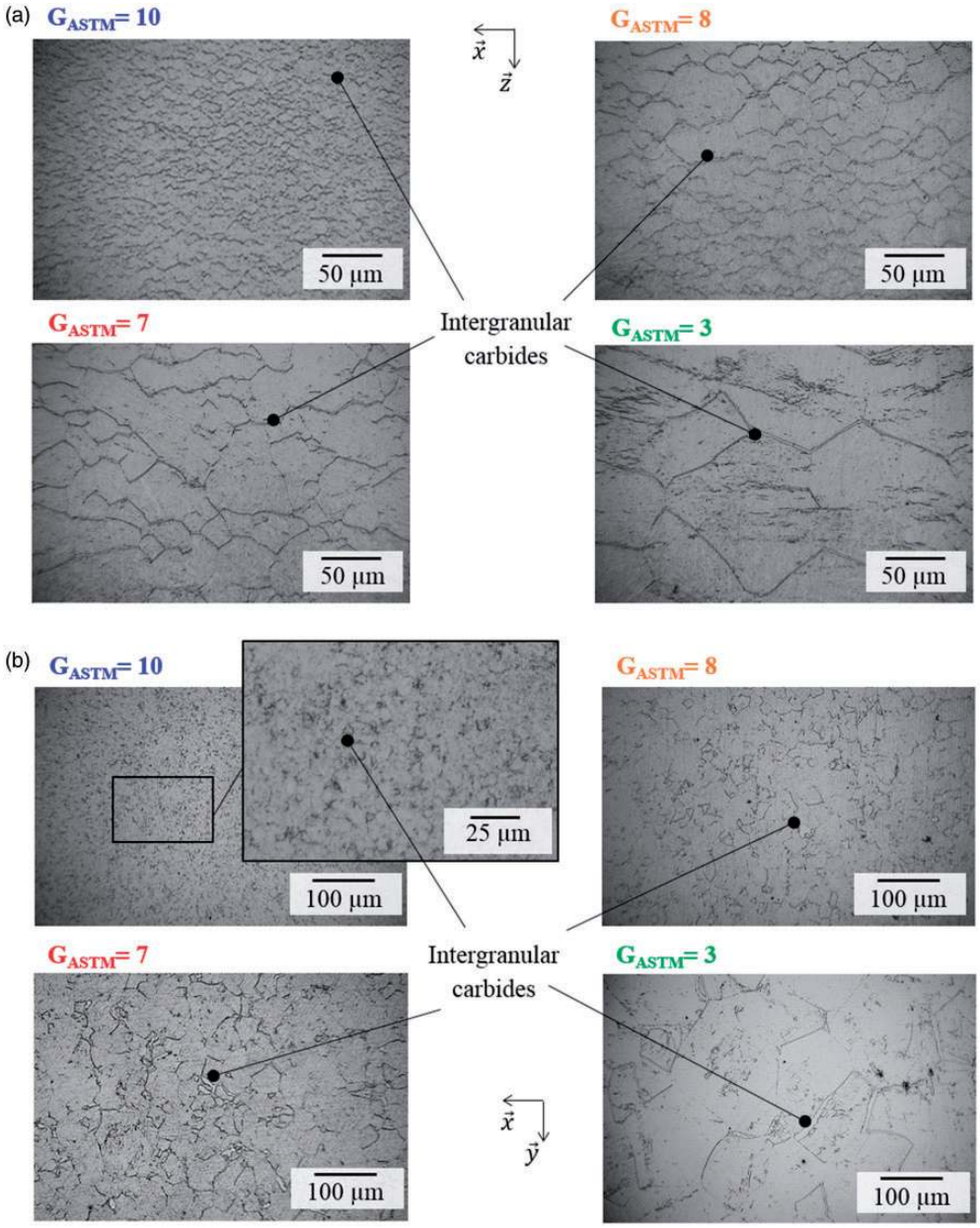

Figure 6. Different morphologies of intergranular carbides within the RCF tested nitrided microstructures (on cross-sections (a) perpendicular and (b) parallel to disc surfaces). $\vec{x}$ and $\vec{z}$ correspond respectively to the rolling and depth directions.

analysed on cross-sections near the contact centre, which are parallel to the rolling direction and perpendicular to disc surfaces (Figure 12). They are prepared according to the methodology described above (section "Metallographic analysis and hardness profile assesments") on damaged volumes displaying the peculiar micropits followed by the surface uplifts (i.e. surface-initiated pitting failure mode).

These observations first confirm that all the experiments reproduced surface-initiated pitting as requested by the adopted experimental strategy (section "Test rig and contact conditions"). Indeed, crack nucleation sites lie near the extreme surfaces at around 30 µm depth and propagation took place beneath, within the nitrided layers. 2D crack morphologies near the contact centre of $G_{ASTM} = 8$ nitrided microstructures studied herein are similar of those observed on $G_{ASTM} = 10$ and $G_{ASTM} = 7$ specimens. They are characterised by large crack lengths reaching great depths up to the untreated substrate of the specimens. In discrepancy with the previous thinner microstructures, surface-initiated pitting on $G_{ASTM} = 3$ disc is generated by superficial crack networks positioned in the vinicity of the extreme surface (less than 80 µm depth). Crack behaviour analysis therefore approves the RCF response differences of $G_{ASTM} = 3$ nitrided microstructures compared with $G_{ASTM} = 10$, $G_{ASTM} = 8$ and $G_{ASTM} = 7$ specimens as

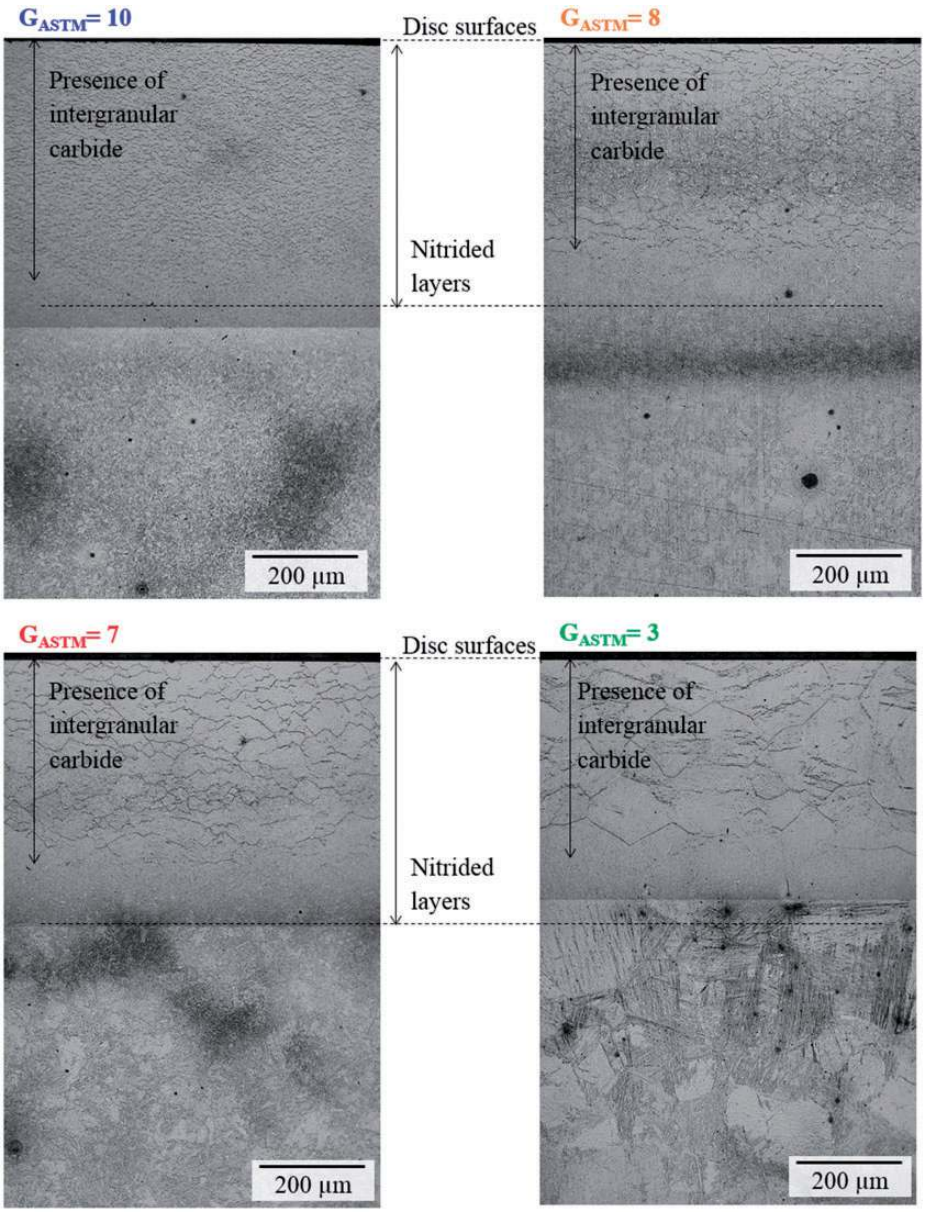

Figure 7. Cross-sections perpendicular to disc surfaces diplaying the RCF tested nitrided microstructures.

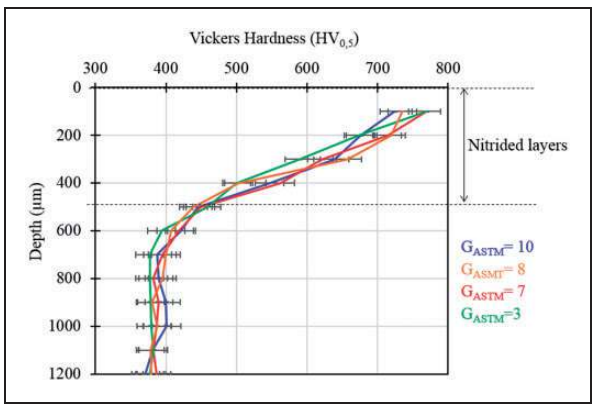

Figure 8. Hardness profiles throughout nitrided cases of RCF tested specimens.

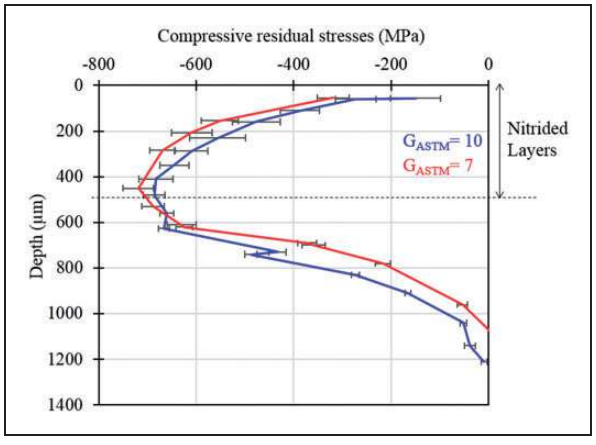

Figure 9. Compressive residual stress profiles throughout nitrided cases of RCF tested specimens.

Table 5. Number of cycles before surface-initiated pitting of different nitrided miscrostructures (tests nos. 1, 3 and 4 are described in Le et al.[11]).

ASTM grain size indexes	$G_{ASTM} = 10$	$G_{ASTM} = 8$	$G_{ASTM} = 7$	$G_{ASTM} = 3$
Number of cycles (10^6)	9.28 (test no. 1)	5.51 (test no. 2)	3.72 (test no. 3)	2.15 (test no. 5)
	/	/	3.69 (test no. 4)	2.86 (test no. 6)

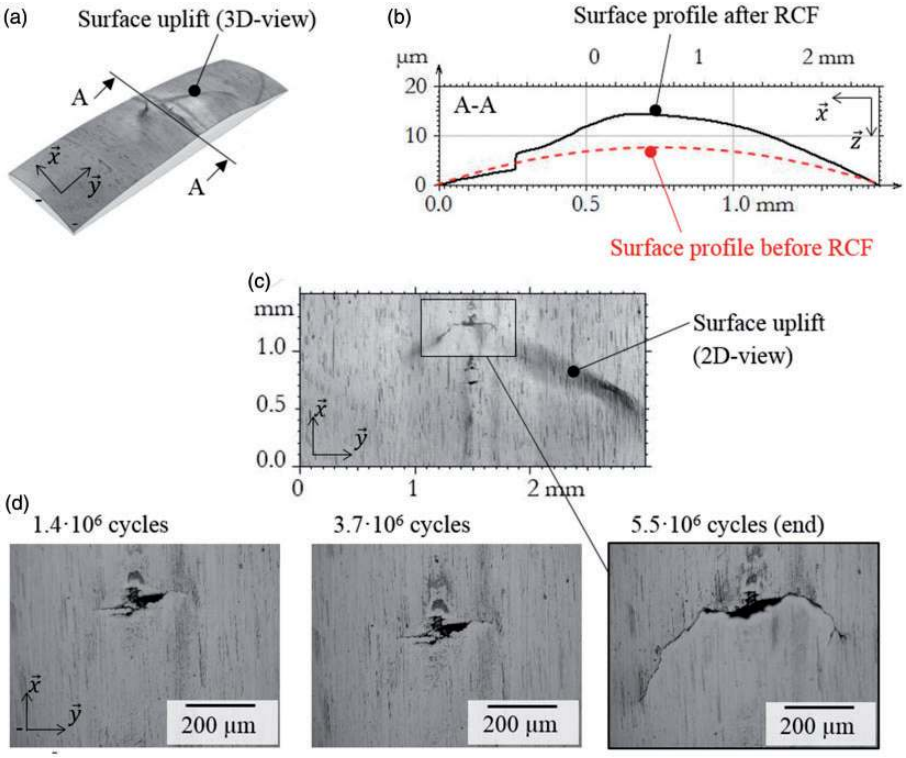

Figure 10. (a) 3D View of a $G_{ASTM} = 8$ specimen (test no. 2) surface in the presence of pitting prior stages (surface uplift); (b) surface profile of pitting prior stages at the contact centre; (c) pitting prior stage surface micrography; (d) surface evolution of RCF damages during fatigue cycling, from micropitting to surface-initiated pitting.

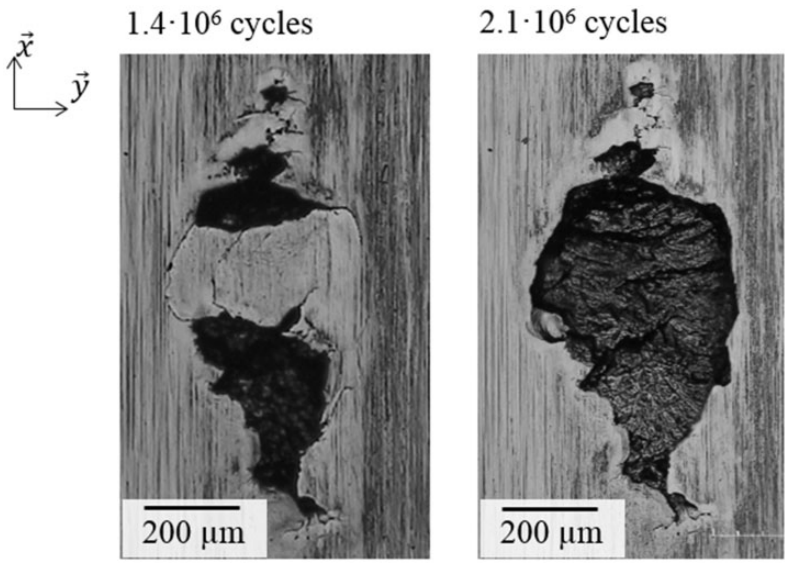

Figure 11. $G_{ASTM} = 3$ specimen (test no. 5) surface evolution of a surface-initiated pitting during fatigue cycling. $\vec{x}$ corresponds to the rolling direction.

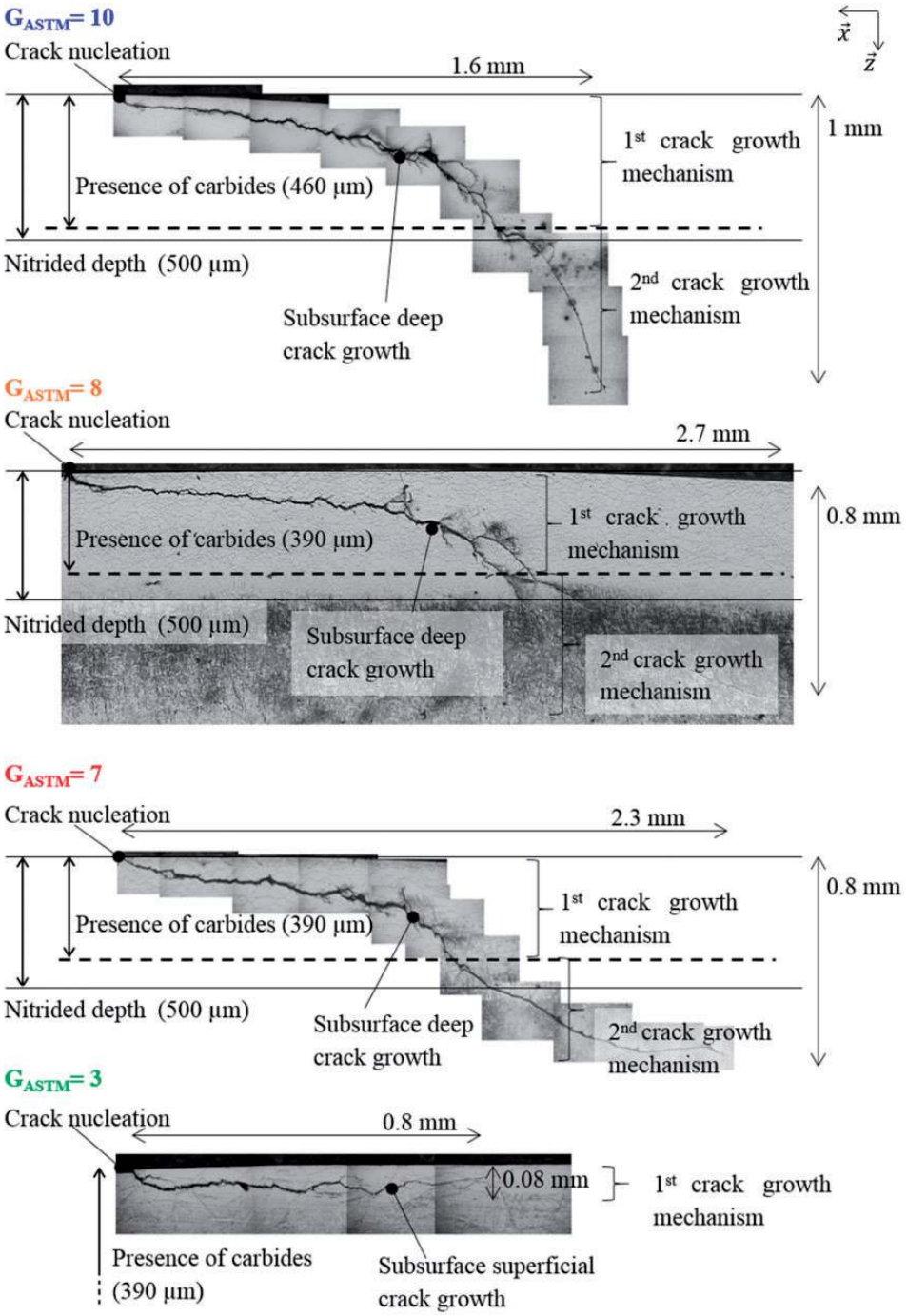

Figure 12. 2D crack morphologies on cross-sections at the contact centre of different nitrided microstructures. $\vec{x}$ and $\vec{z}$ correspond respectively to the rolling and depth directions.

foreseen above with disc surface examinations (section "Endurances of the tested nitrided microstructures").

Observations of etched micrographs with higher magnifications show lots of intergranular carbides along the crack paths (Figure 13), as if those precipitates act as heterogeneities favouring crack growth. Cracks are notably observed propagating either at the interface between the ferritic matrix and the carbides, either shearing directly the precipitates, which appear as fragile.

Considering these intergranular carbides induced by gas-nitriding as preferential sites for crack growth, the RCF response encountered in $G_{ASTM} = 3$ in contrast to the other microstructures could thus be explained. Indeed, $G_{ASTM} = 3$ nitrided microstructures display low density of intergranular carbides which are far from each other with respect to the normal direction of the surface (Figure 6(a)). In that sense, cracks could not propagate throughout the nitrided layers toward the untreated substrate since

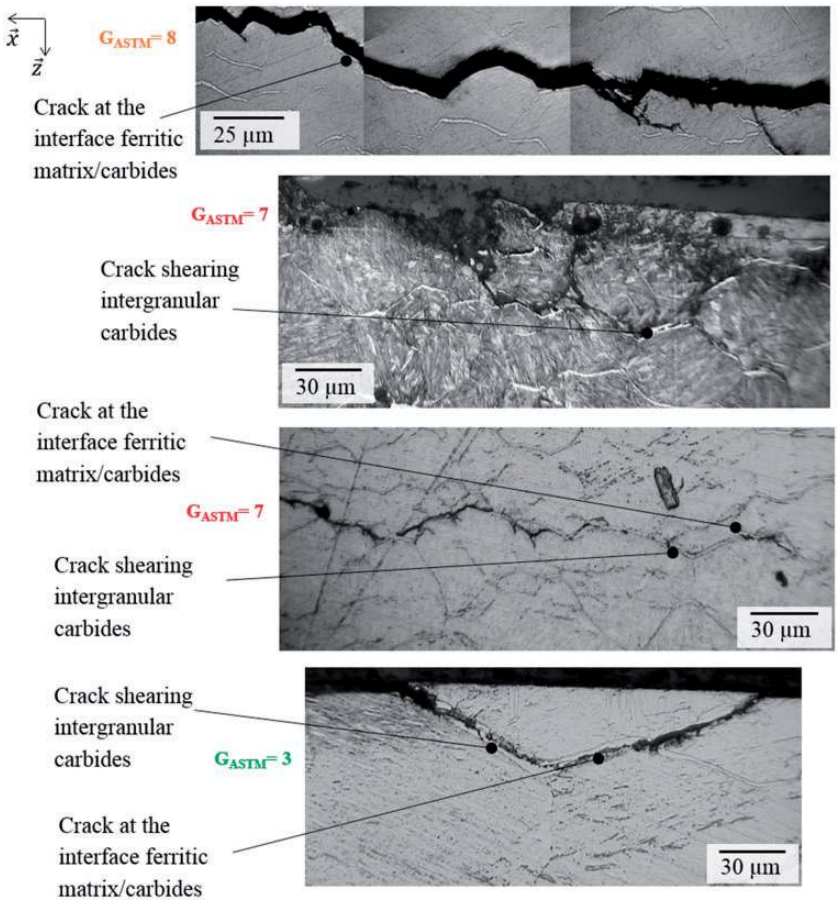

Figure 13. Cracks propagating at the interfaces ferritic matrix/carbides, or shearing the intergranular carbides.

intragranular crack growth seems to require more energy than crack propagation through the carbides.

For those $G_{ASTM} = 3$ specimens (Figure 12, $G_{ASTM} = 3$), surface-initiated pitting therefore comes from superficial cracks that only propgate very close to the extreme surface. On the contrary, thinner nitrided microstructures are characterised by higher density of carbides which are close to each other (Figure 6(a)). The intergranular precipitates form a bridge from the surface (where cracks were nucleated by indented counter discs during the initiation phase) and the substrate of the specimens, dragging cracks in depth during fatigue loading. In that case, thin nitrided microstructures provoke surface-initiated pitting formed by deep crack propagation (Figure 12, $G_{ASTM} = 10$, $G_{ASTM} = 8$, $G_{ASTM} = 7$). It should be noted that even if some portions of crack paths are not bordered by the carbides, previous study[11] has shown that 2-D crack analysis on a unique cross-section could engender misleading interpretations. Examinations of successive cross-sections obtained by thin polishing (around 10 µm material removal between each plane) effectively highlight possible 3D crack propagation along carbides in adjacent parallel planes.

Finally, analysis of the whole crack paths on cross-sections near the contact centre show two fracture mechanisms (Figure 12). The first one stands out as an irregular pattern as are the intergranular carbides where cracks went through. The second one is illustrated by a fracture surface much smoother as if cracks were no more affected by the microstructure. Moreover, the limit between those crack growth mechanisms is located at the limit of the presence of the intergranular precipitates induced by gas-nitriding within the treated layers. These observations therefore support the statement that the carbides affect RCF crack propagation. They are fragile sites where cracks propagate more easily throughout the nitrided layers.

3D observations of the crack network: Carbide effect confirmation

To complete 2D analysis on cross-sections near the contact centre, 3D observations of a crack network in a RCF tested GASTM = 7 specimen (test no. 3 in Table 5) were carried out using high-resolution X-ray tomography (section ''3D observation using high-resolution X-ray computed tomography''). Figure 14 illustrates half part of a 3D crack network induced by RCF. It is apparently characterised by two fracture surfaces, as observed on 2D cross-sections, referring therefore to two RCF crack mechanisms within the

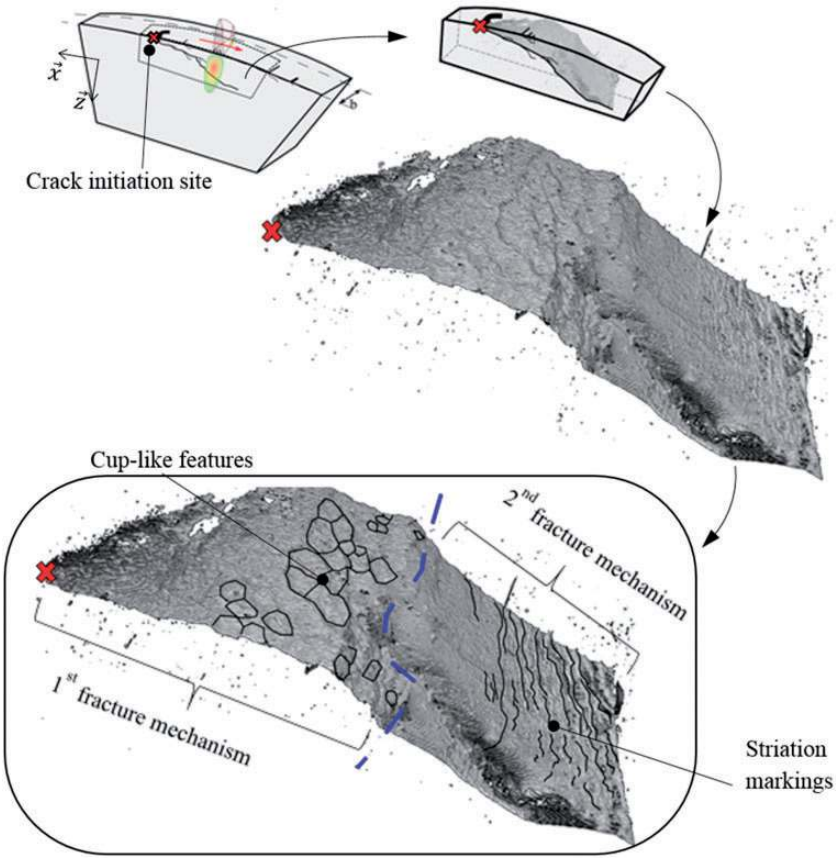

Figure 14. Half part of a RCF crack network displaying two different fracture surfaces.

nitrided layers. The first fracture surface closest to the surface displays cup-like features while the deeper fracture surface in the nitrided layer appears with fatigue striation-like markings.

The cup-like fracture surface seems to match with the intergranular carbide 3D morphology. Indeed, those carbides precipitated during nitriding on grain boundaries more or less parallel to the surface and form dented coats that cover up to five grains. Considering cracks going through those carbides in all the directions, they therefore generate the cup-like fracture surface. To confirm this assumption, it is necessary to compare dimensions of the cup-like features to those of the carbides. Collected datas from X-ray tomography are post-processed in another way to get the cup-like feature dimensions. Namely, 2D scanned images parallel to the disc surface were superposed. This results in an image illustrated on Figure 15(b), which is merely similar to an observation of the 3D crack network from the underside, through the plane parallel to the surface sketched in green (Figure 15(a)), with a large depth of field.

This figure is replicated in Figure 15(c), where cup-like features and striation markings are highlighted. The mean cup-like feature dimensions can thus be estimated and compared with those of the intergranular carbides assessed on cross-sections parallel to the surface. One of those cross-sections, depicted in Figure 16(a), shows that evaluated dimensions of cup-like features and intergranular carbides are comparable. This last assessment supports once again the effect of carbides induced by nitriding on the crack propagation mechanism within the treated layers. Indeed, cracks grow through or along those carbides forming specific cup-like fracture surface.

Pre-existing compressive residual stress release

Compressive residual stress (CRS) were measured throughout nitrided depths after RCF testing on disc samples not displaying surface-initiated pitting. The results are compared with the CRS profile before fatigue (Figure 17).

The curves show differences throughout the treated layers. From the surface ($z = 0\,\mu m$) to $z = 500\,\mu m$ depth, CRS after fatigue are less compressive than before the tests, whilst beneath $z = 500\,\mu m$ depth the CRS are more compressive after RCF. In the literature,[23–25] sub-surface CRS buildup were observed on through-hardened steels (100Cr6 for instance) at depth were shear stresses induced by the contact are important with respect to the material yield strength. This phenomenon was assumed to be linked to volume variation provoked by microstructural decay development in the presence of stresses arising from the contact. Metallographic analysis were therefore

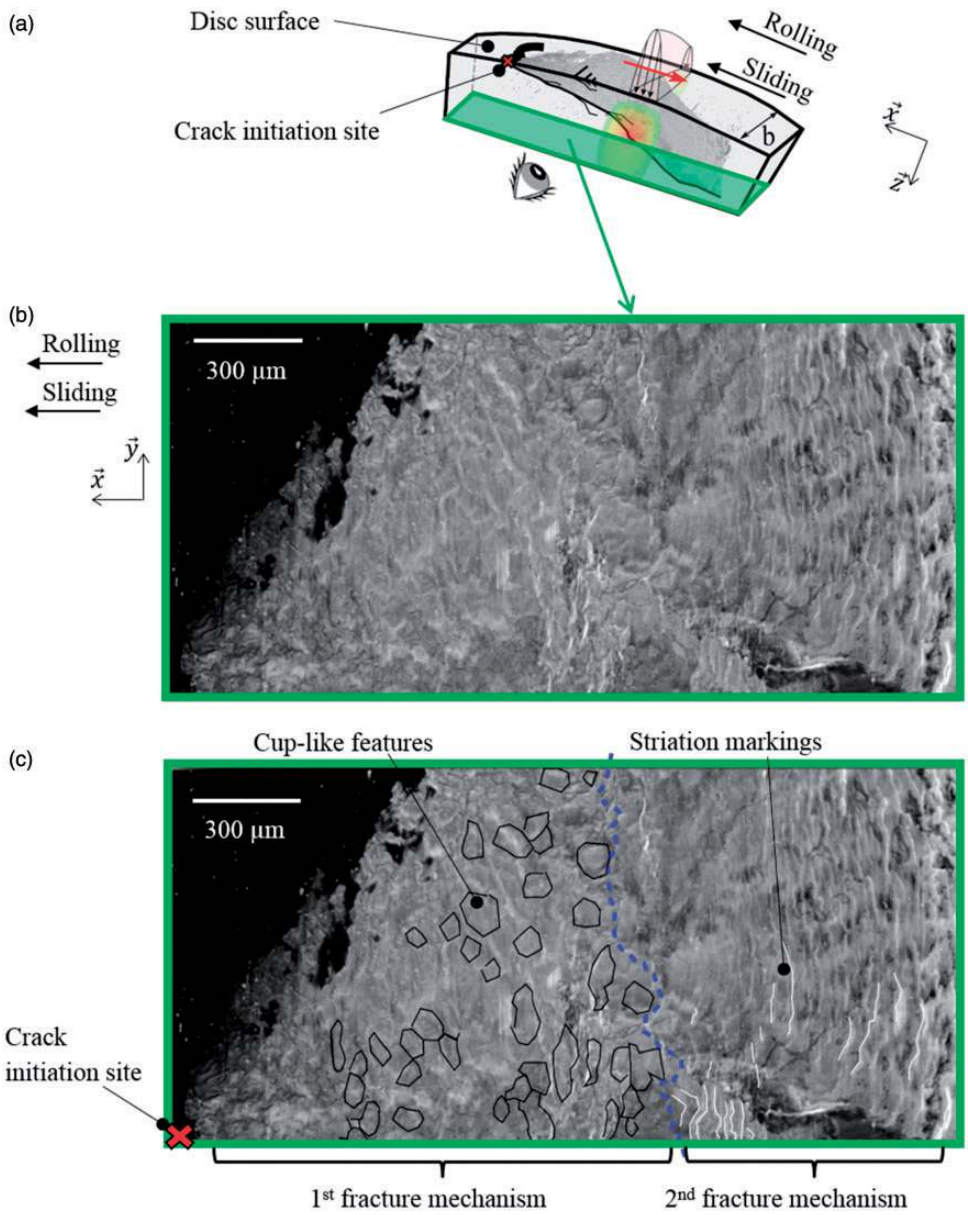

Figure 15. (a) Scheme of the sample analysed by X-ray tomography. (b) Resulting image of supperposition of the 2D scanned images parallel to disc surface showing (c) the two fracture mechanisms. $\vec{x}$ and $\vec{z}$ correspond respectively to the rolling and depth directions.

performed on the tested specimens seeking for apparent microstructural alterations within the nitrided layers (Figure 18).

Etching cross-sections with Béchet-Beaujard reveals darker areas against the unstrained microstructure appearance. At higher magnifications, these dark areas display thin stroke markings, which are likely related with the slip band structures, features of micro-plastic flow concentration during fatigue cycling and widely discussed in the literature as dark etching regions (DER).[24,26] Observations of cross-sections perpendicular to rolling direction (Figure 18(b)) confirms those slip bands being induced by cyclic contact loading since the dark area shape corresponds thoroughly to the pattern of the contact shear stress field.

It therefore seems that during fatigue cycling, the specimens were subjected to micro-plastic deformation accumulation at Hertzian depths where contact shear stresses are important. This microstructural decay provoked volume variation at the origin of sub-surface (beneath $z = 500\,\mu m$ depth) additional compressive residual stress buildup. Finally, from the surface ($z = 0\,\mu m$ depth) to $z = 500\,\mu m$ depth, it can be presumed that pre-existing CRS (resulted from the thermochemical nitriding heat treatment) had to release so as to accommodate volume variation. In other words, final CRS measured profile differs from the one before RCF tests because (1) contact shear stresses lead to microplastic deformation engendering, (2) sub-surface additional CRS buildup which provokes (3) pre-existing CRS release.

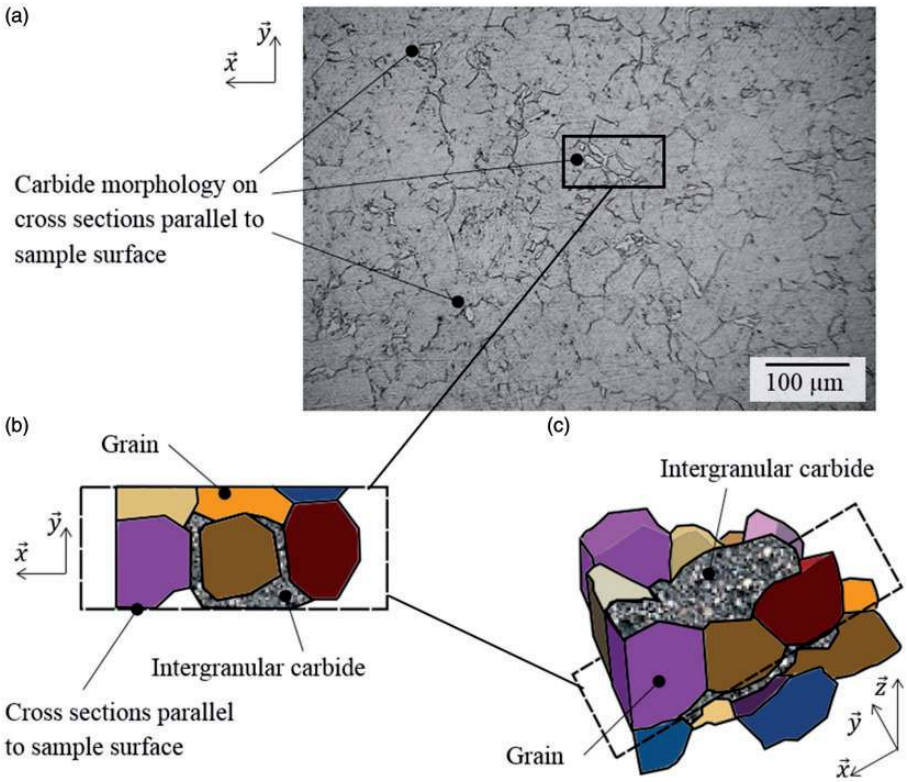

Figure 16. (a) $G_{ASTM} = 7$ nitrided layer microstructure on cross-section parallel to the surface. (b) Scheme of a cross-section parallel to the sample surface. (c) Scheme of the 3D nitrided microstructure. $\vec{x}$ and $\vec{z}$ correspond respectively to the rolling and depth directions.

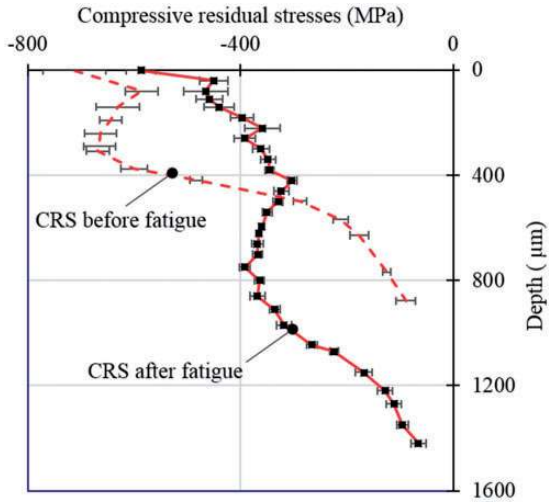

Figure 17. Compressive residual stress profiles before and after fatigue cycling.

RCF test results at $P_{Hmax} = 1.2$ GPa and $P_{Hmax} = 2.4$ GPa: Compressive residual stress behaviour in relation to contact shear stress field

Pre-existing CRS induced by nitriding realeased during RCF tests at $P_{Hmax} = 2.1$ GPa. Other experiments were performed to observe the CRS behaviour on specimens undergoing RCF at other Hertzian pressures. Only $G_{ASTM} = 7$ nitrided specimens were tested at $P_{Hmax} = 1.2$ GPa and $P_{Hmax} = 2.4$ GPa. After more than $10 \times \cdot 10^6$ cycles, none of the micropits on these nitrided specimens have extended to pitting as arised on previous tests with $P_{Hmax} = 2.1$ GPa at about $3.6 \times \cdot 10^6$ cycles (Table 5). Moreover, after RCF only few persistent slip bands were noticed on cross-sections of the specimens (Figure 19) compared with those tested at $P_{Hmax} = 2.1$ GPa (Figure 18). Even if the maximum contact shear stress level is higher ($\tau_{max} = 744$ MPa at $P_{Hmax} = 2.4$ GPa compared with $\tau_{max} = 630$ MPa at $P_{Hmax} = 2.1$ GPa, Figure 1), microplastic flow had not developed as much as on specimens subjected to $P_{Hmax} = 2.1$ GPa.

Compared with these first experiments at $P_{Hmax} = 2.1$ GPa where microplastic deformation seemed to trigger CRS buildup at maximum contact shear stresses and therefore pre-existing CRS release, none of these phenomenon occurred on tests performed at $P_{Hmax} = 1.2$ GPa nor $P_{Hmax} = 2.4$ GPa. Pre-existing CRS being unaltered, the nitrided layers remain in a compressive stress state which could have prevented propagation of surface-initiated cracks that are freezed close to the specimen surfaces. Finally, initiated micropits did not extend to pitting failure mode.

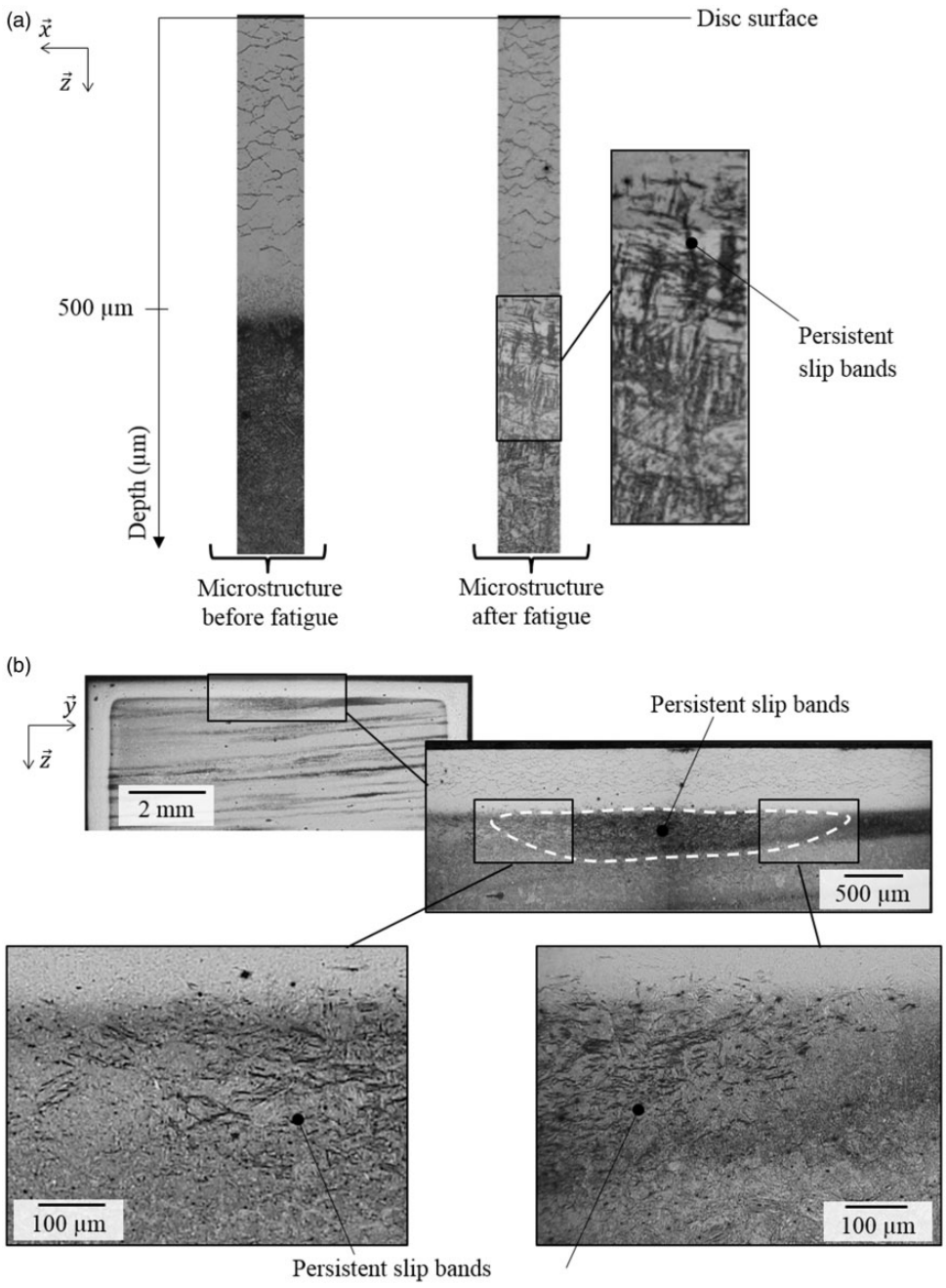

Figure 18. Cross-sections (a) parallel and (b) perpendicular to the rolling direction revealing the presence of persistent slip bands at high stressed zones in the specimens after RCF.

It is to be noticed that $\tau_{max} = 744$ MPa (induced by $P_{Hmax} = 2.4$ GPa) is located (Figure 1) in the nitrided layers where compressive residual stresses and hardness are relatively high (Figure 8 and Figure 9). In contrast, $\tau_{max} = 630$ MPa (induced by previous tests at $P_{Hmax} = 2.1$ GPa) takes place at the limit of the nitrided case where mechanical properties are lower and equivalent to those of the substrate. The nitrided layers being featured by microstructural and mechanical property variation throughout the depth, it therefore seems that RCF mechanisms depend on the local contact stress field characteristics (maximum shear stress value and depth, etc.) in relation to the local properties of the material.

Discussion: Surface-initiated pitting mechanisms within nitrided alloyed steels with respect to contact stresses

Considering all of the experiments, RCF mechanisms of nitrided layers of alloyed steels maybe be suggested with respect to their microstructural and mechanical properties, but also the contact shear stresses. These suggestions can be applied to components involing

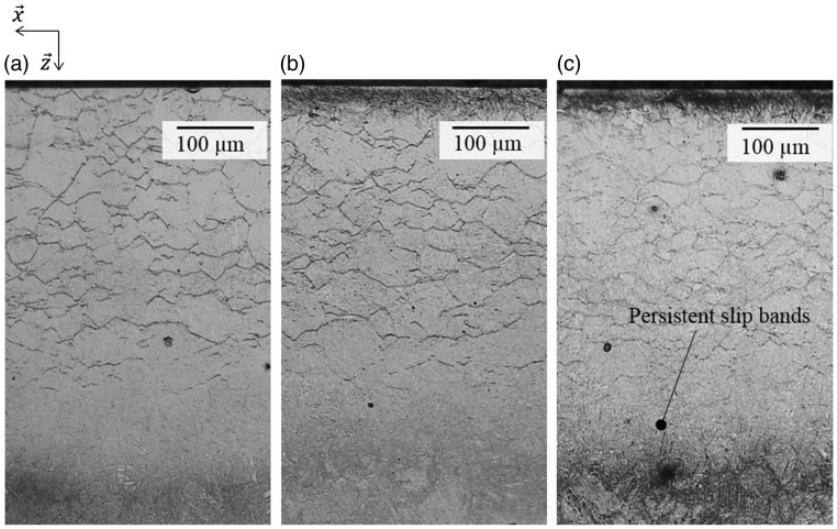

Figure 19. Cross-sections of (a) non-tested specimens and tested at (b) $P_{Hmax} = 1.2$ GPa and (c) $P_{Hmax} = 2.4$ GPa revealing the presence of few persistent slip bands only on tested specimens at $P_{Hmax} = 2.4$ GPa.

mechanical contacts, with defects at their surfaces (i.e. stress raisers such as debris dents, micropitting, etc. that have nucleated superficial cracks).

During RCF, if local contact shear stresses are critical compared with local material strength (either within the nitrided layer or within the core), microplastic deformation takes place. This phenomenon first engenders CRS buildup where deformation occurs as observed in the literature on other throught hardened steels tested in RCF.[23–25] This CRS buildup and microplastic flow release (by deformation accomodation) elsewhere pre-existing CRS introduced by the nitriding process. This pre-existing CRS release phenomenon in nitrided layers due to RCF has not been observed in the literature to the author knowledge. Once residual stresses are less compressive, cracks that were initiated near the extreme surface are relieved at their tips. They can therefore propagate preferentially along fragile sites like the intergranular carbides introduced by the thermomechanical treatment. Their specific morphology and the contact stresses drag surface-initiated cracks toward the core in thin nitrided microstructures, forming specific fracture surfaces in correlation with the carbide shape within the nitrided layers. In coarser nitrided microstructures, intergranular carbide networks are in low density and the precipitates are far from each other with respect to the normal direction to the surface. Cracks could not propagate throughout the coarse microstructure nitrided layers toward the untreated substrate since intragranular crack growth seems to require more energy than crack propagation through the carbides. Intergranular carbides can therefore be considered as fragile sites for crack growth as indicated without noticeable evidences in the literature so far. In thin nitrided microstructures that are in accordance with the gear material quality standard,[21] surface-initiated cracks lead to deep pitting failures, whereas they engender superficial pits in coarser microstructures even if mechanical properties are equivalent. Coarser microstructures could first appear greater according to gear material quality standart for example. Surface-initiated pitting defect durability is however to be taken into account since the failures occur sooner in those coarse nitrided microstructures.

Conclusion

Effect of nitrided depth and hardness profile parameters on RCF endurances being widely analysed in the literature, this study points out the major roles of the nitrided microstructures and the CRS behaviour. Even though hardness increase and CRS introduction by the nitriding process within the thin and superficial treated layers are known to inhibit fatigue crack nucleation and growth, it was observed herein that if initial CRS releases, cracks can grow and their propagation paths highly depend on the microstructure. This explains the RCF behaviour dissimilarities of different nitrided layers displaying different carbide network morphologies but similar mechanical properties (hardness and CRS).

Pre-existing CRS release can indeed occur by accomodation of additional CRS buildup induced by RCF microplastic deformation arising elsewhere in the nitrided layers where local contact stresses are critical compared with the local mechanical properties of the material. If this phenomenon takes place in a treated layer in the presence of defects such as surface-initiated cracks, their tips are freed leading to crack propagation preferentially along the fragile intergranular carbides generated by nitriding. These phenomenom result in

the surface initiated-pitting failure mode that gears and rolling element bearings can encounter.

From an industrial point of view, case depths and hardness profiles within the nitrided layers being easily assessed, they constitute the parameters that are mainly checked for the validation of the mechanical component material quality. This study highlights the importance of adjusting microstructural and mechanical properties of nitrided layers in relation to the operating contact conditions of the final application.

Declaration of Conflicting Interests

The author(s) declared no potential conflicts of interest with respect to the research, authorship, and/or publication of this article.

Funding

The author(s) disclosed receipt of the following financial support for the research, authorship, and/or publication of this article: The authors would like to express their gratitude to the DCNS group, the DGA and the ANRT for their financial support and to Bodycote group for the specimen nitriding.

References

1. Suresh S. *Fatigue of materials*. Cambridge solid state science series. Cambridge: Cambridge University Press, 1998.
2. Johnson KL. *Contact mechanics*. Cambridge: Cambridge University Press, 1987.
3. Kaneta M, Suetsugu M and Murakami Y. Mechanism of surface crack-growth in lubricated rolling sliding spherical contact. *J Appl Mech* 1986; 53: 354–360.
4. Meheux M, Minfray C, Ville F, et al. Effect of lubricant additives in rolling contact fatigue. *Proc IMechE, Part J: J Engineering Tribology* 2010; 224: 947–955.
5. Ruellan A, Ville F, Kleber X, et al. Understanding white etching cracks in rolling element bearings: The effect of hydrogen charging on the formation mechanisms. *Proc IMechE, Part J: J Engineering Tribology* 2014; 228: 1252–1265.
6. Voskamp AP. Material response to rolling contact loading. *J Tribol* 1985; 107: 359–364.
7. Schlicht H, Schreiber O and Zwirlein E. Effects of material properties on bearing steel fatigue strength. In: *Effect of steel manufacturing processes on the quality of bearing steels*. West Conshohocken, PA: ASTM International, 1988.
8. Olver AV, Cole SJ and Sayles RS. Contact stresses in nitrided steels. In: *Proceedings of 19th Leeds-Lyon symposium on tribology*, Leeds, 1993.
9. Wilkinson CMR and Olver AV. The durability of gear and disc specimens - part i: The effect of some novel materials and surface treatments. *Tribol Trans* 1999; 42: 503–510.
10. Barrallier L, Traskine V and Botchenkov S. Morphology of intergranular cementite arrays in nitrided chromium-alloyed steels. *Mater Sci Eng A* 2005; 393: 247–253.
11. Le M, Ville F, Kleber X, et al. Influence of grain boundary cementite induced by gas nitriding on the rolling contact fatigue of alloyed steels for gears. *Proc IMechE, Part J: J Engineering Tribology* 2015.
12. Ville F, Nélias D, Tourlonias G, et al. On the two-disc machine: A polyvalent and powerful tool to study fundamental and industrial problems related to elastohydrodynamic lubrication. *Tribology series*. vol. 39, New York: Elsevier, 2001, pp.393–402.
13. Diab Y, Coulon S, Ville F, et al. Experimental investigations on rolling contact fatigue of dented surfaces using artifical, defects: Subsurface analyses. In: Dalmaz G, Dowson D, Priest M, Lubrecht AA (eds) In: *Tribological research and design for engineering systems proceedings of the 29th Leeds-Lyon symposium on tribology*, Vol. 41 of Tribology Series, 2003, pp.359–366. New York: Elsevier.
14. Coulon S, Jubault I, Lubrecht AA, et al. Pressure profiles measured within lubricated contacts in presence of dented surfaces. comparison with numerical models. *Tribol Int* 2002; 37: 111–117.
15. Ville F, Coulon S and Lubrecht AA. Influence of solid contaminants on the fatigue life of lubricated machine elements. *Proc IMechE, Part J: J Engineering Tribology* 2006; 220: 441–445.
16. Labiau A, Ville F, Sainsot P, et al. Effect of sinusoidal surface roughness under starved conditions on rolling contact fatigue. *J Eng Tribol* 2008; 222: 193–200.
17. Fabre A, Evans HP, Barrallier L, et al. Prediction of microgeometrical influences on micropitting fatigue damage on 32crmov13 steel. *Tribol Int* 2013; 59: 129–140.
18. Martins R, Locatelli C and Seabra J. Evolution of tooth flank roughness during gear micropitting tests. *Ind Lubric Tribol* 2011; 63: 34–45.
19. Kaneta M, Yatsuzuka H and Murakami Y. Mechanism of crack growth in lubricated rolling/sliding contact. *ASLE Trans* 1985; 28: 407–414.
20. Buffière J-Y, Proudhon H, Ferrie E, et al. Three dimensional imaging of damage in structural materials using high resolution micro-tomography. *Nucl Instrum Methods Phys Res B* 2005; 238: 75–82.
21. ISO 6336-5. *Calculation of load capacity of spur and helical gears - Part 5: Strength and quality of materials* 2003.
22. Jegou S. *Influence des éléments d'alliage sur la genèse des contraintes résiduelles d'aciers nitrurés*. PhD Thesis, Arts et Métiers ParisTech, France, 2009.
23. Muro H and Tsushima N. Microstructural, microhardness and residual stress changes due to rolling contact. *Wear* 1970; 15: 309–330.
24. Voskamp AP. *Fatigue and material response in rolling contact*. New York: American Society for Testing and Materials, 1998.
25. Sadeghi F, Jalalahmadi B, Slack TS, et al. A review of rolling contact fatigue. *J Tribol* 2009; 131/041403: 1–15.
26. Bhadeshia HKDH. Steels for bearings. *Prog Mater Sci* 2012; 57: 268–435.